Spin-state transition and phase separation in a multiorbital Hubbard model

Ryo Suzuki,[1,*] Tsutomu Watanabe,[2,†] and Sumio Ishihara[1]
[1]*Department of Physics, Tohoku University, Sendai 980-8578, Japan*
[2]*Institute of Multidisciplinary Research for Advanced Materials, Tohoku University, Sendai 980-8577, Japan*
(Received 9 May 2009; revised manuscript received 26 June 2009; published 18 August 2009)

We study the spin-state transition and the phase separation involved in this transition based on the multiorbital Hubbard model. Multiple spin states are realized by changing the energy separation between two orbitals and the on-site Hund coupling. By utilizing the variational Monte-Carlo simulation, we analyze the electronic and magnetic structures in hole doped and undoped states. Electronic phase separation occurs between the low-spin band insulating state and the high-spin ferromagnetic metallic state. The difference in the band widths of the two orbitals is of prime importance for the spin-state transition and the phase separation.

DOI: 10.1103/PhysRevB.80.054410 PACS number(s): 75.25.+z, 71.70.−d, 71.30.+h

I. INTRODUCTION

Exotic electric and magnetic phenomena observed in correlated electron systems are responsible for competition and cooperation between multielectronic phases with delicate energy balances. These phenomena arise due to the internal degrees of freedom of electrons, i.e., spin, charge and orbital, under strong electron correlation, and their coupling with the lattice.[1,2] In some transition-metal ions, there is an additional degree of freedom termed the spin-state degree of freedom, i.e., multiple spin states due to the different electron configurations in a single ion. A prototypical example is the perovskite cobaltites $R_{1-x}A_xCoO_3$ (R: rare earth ion, A: alkaline earth ion) where transitions between the multiple spin states occur by changes in the carrier concentration, temperature and other parameters. In Co^{3+} with a d^6 configuration, there are three possible spin states, the high-spin (HS) state $(e_g^2t_{2g}^4)$ with an amplitude of $S=2$, the intermediate-spin (IS) state $(e_g^1t_{2g}^5)$ with $S=1$, and the low-spin (LS) state (t_{2g}^6) with $S=0$.

Several magnetic, electric, and transport measurements have been done in insulating and metallic cobaltites. It is known that $LaCoO_3$ is a nonmagnetic LS band insulator (BI) at low temperatures, although there is still controversy over the spin-state transition and the IS state at finite temperature.[3–7] In the high hole doping region of $x>0.3-0.4$ in $La_{1-x}Sr_xCoO_3$, a ferromagnetic (FM) metallic state was experimentally confirmed. In the lightly hole-doped region between the LS BI and FM metallic states, several inhomogeneous features in the magnetic, electric and lattice structures have been reported experimentally. Spatial segregation of the hole-rich FM and hole-poor insulating regions have been suggested by neutron diffraction, electron microscopy, NMR and other studies.[8–11] Magnetic–nonmagnetic clusters have been found by small-angle and inelastic neutron scattering experiments.[12–14] It is widely believed that the observed giant magnetoresistance effect in the lightly doped region results from electronic and magnetic inhomogeneity.[12]

Electronic phase separation (PS) phenomena in transition-metal compounds have been studied extensively and intensively, in particular in high-Tc superconducting cuprates and colossal magnetoresistive manganites.[15–20] In these materials, the long-range spin/orbital orders in the Mott insulating phases and their melting by carrier doping are essential for the electronic PS. The exchange energy for the localized spins/orbitals and the kinetic energy of the itinerant electrons are gained in spatially separate regions. On the contrary, in the present case, a nonmagnetic BI is realized in the insulating phase and a spin-state transition is brought about by carrier doping. Thus, the present phenomena belong to a new class of electronic PS in correlated systems, although only a few theoretical studies have been done to date. In this paper, we address the issues of the spin-state transition and the PS associated with this transition by analyzing the multiorbital Hubbard model. We examine the electronic structures in hole doped and undoped systems by the variational Monte-Carlo (VMC) method. We find that the electronic PS is realized between the nonmagnetic BI and the HS FM metal. We conclude that the different band widths play an essential role in the present electronic PS. In Sec. II, the model Hamiltonian and the VMC method are introduced. Numerical results and discussions are presented in Sec. III.

II. MODEL

We have considered a minimal model, the two-orbital Hubbard model,[21–24] to examine the spin-state degrees of freedom and the transition between them. In each site in a crystal lattice, we consider two orbitals, termed A and B, which represent one of the e_g and t_{2g} orbitals, respectively. An anisotropic shape of the orbital wave function is not considered. The energy difference between the two orbitals is denoted by $\Delta \equiv \varepsilon_A - \varepsilon_B > 0$ where ε_A and ε_B are the level energies for A and B. When the electron number per site is two, the lowest two electronic states in a single site are $|B^2\rangle$ and $|A^1B^1\rangle$ which form a spin triplet state, termed the LS and HS states in the present model, respectively. The explicit form of the model Hamiltonian is given by

$$\mathcal{H} = \Delta \sum_{i\sigma} c^\dagger_{iA\sigma} c_{iA\sigma} - \sum_{\langle ij\rangle\gamma\sigma} t_\gamma (c^\dagger_{i\gamma\sigma} c_{j\gamma\sigma} + \text{H.c.}) + U \sum_{i\gamma} n_{i\gamma\uparrow} n_{i\gamma\downarrow} + U' \sum_{i\sigma\sigma'} n_{iA\sigma} n_{iB\sigma'} - J \sum_{i\sigma\sigma'} c^\dagger_{iA\sigma} c_{iB\sigma} c^\dagger_{iB\sigma'} c_{iA\sigma'} - J' \sum_{i\gamma} c^\dagger_{i\gamma\uparrow} c_{i\bar{\gamma}\uparrow} c^\dagger_{i\gamma\downarrow} c_{i\bar{\gamma}\downarrow}, \quad (1)$$

where $c_{i\gamma\sigma}$ is the annihilation operator of an electron at site i in orbital $\gamma(=A,B)$ and with spin $\sigma(=\uparrow,\downarrow)$, and $n_{i\gamma\sigma} \equiv c^{\dagger}_{i\gamma\sigma}c_{i\gamma\sigma}$ is the number operator. The subscript $\bar{\gamma}$ takes A or B, when γ is B or A, respectively. We assume that the transfer integral is diagonal with respect to the orbitals and $|t_A| > |t_B|$; both assumptions being justified in perovskite cobaltites. In most of the numerical calculations, the relation $t_B/t_A=1/4$ is chosen. For intra-site electron interactions, we consider the intra- and interorbital Coulomb interactions, U and U', respectively, the Hund coupling J and the pair-hopping J'. The relations $U=U'+2J$ and $J=J'$ satisfied in an isolated ion are assumed. In addition, we consider the relation $U=4J$ in the numerical calculation.

We adopt the VMC method where simulations for a large cluster size are possible. For simplicity, and to limit computer resource requirements, we use two-dimensional square lattices with a system size of $N \equiv L^2 (L \leq 8)$ with periodic and antiperiodic boundary conditions. The number of electrons is N_e and the hole concentration per site, measured from $N_e=2N$, is denoted as $x \equiv (2N-N_e)/N$. The variational wave function is given as the product $\Psi = G|\Phi\rangle$ where G is the correlation factor and $|\Phi\rangle$ is the one-body wave function. Two types of wave function are considered in $|\Phi\rangle$. (1) The Slater determinant given as

$$|\Phi_N\rangle = \prod_{\mathbf{k}}{}' \prod_{\gamma\sigma} c^{\dagger}_{\mathbf{k}\gamma\sigma}|0\rangle, \tag{2}$$

where $c_{\mathbf{k}\gamma\sigma}$ is the Fourier transform of $c_{i\gamma\sigma}$, and $\Pi'_{\mathbf{k}}$ is a product of $\mathbf{k}$ up to the Fermi momentum for the bands which is obtained from the first and second terms in Eq. (1). (2) The wave function for the HS antiferromagnetic (AFM) order given as

$$|\Phi_{AF}\rangle = \prod_{\mathbf{k}}{}'' \prod_{\gamma\sigma} d^{\dagger}_{\mathbf{k}\gamma\sigma} d^{\dagger}_{\mathbf{k}+\mathbf{K}\gamma\sigma}|0\rangle, \tag{3}$$

where

$$d^{\dagger}_{\mathbf{k}\gamma\sigma} = \alpha^{(+)}_{\mathbf{k}\gamma} c^{\dagger}_{\mathbf{k}\gamma\sigma} + \varsigma_{\sigma}\alpha^{(-)}_{\mathbf{k}\gamma} c^{\dagger}_{\mathbf{k}+\mathbf{K}\gamma\sigma}, \tag{4}$$

and

$$d^{\dagger}_{\mathbf{k}+\mathbf{K}\gamma\sigma} = -\varsigma_{\sigma}\alpha^{(-)}_{\mathbf{k}\gamma} c^{\dagger}_{\mathbf{k}\gamma\sigma} + \alpha^{(+)}_{\mathbf{k}\gamma} c^{\dagger}_{\mathbf{k}+\mathbf{K}\gamma\sigma}, \tag{5}$$

where $\mathbf{K}=(\pi,\pi)$ and $\Pi''_{\mathbf{k}}$ represents a product of $\mathbf{k}$ up to the Fermi momentum in the first AFM Brillouin zone. We have $\varsigma_{\uparrow(\downarrow)}=1(-1)$ and

$$\alpha^{(\pm)}_{\mathbf{k}\gamma} = \frac{1}{\sqrt{2}}\sqrt{1 \mp \frac{e_{\mathbf{k}\gamma}}{\sqrt{e^2_{\mathbf{k}\gamma}+\Delta^2_{\mathrm{AF}}}}}, \tag{6}$$

where $e_{\mathbf{k}\gamma}$ is the eigenenergy for the first and second terms in Eq. (1), and Δ_{AF} is a variational parameter for the AFM order. We assume the Gutzwiller-type correlation factor $\Pi_{il}(1-\xi_l \mathcal{P}_{il})$ where l indicates the local electron configurations, $\mathcal{P}_{il}$ is the projection operator at site i for the configuration l, and ξ_l is the variational parameter. We adopt 10 variational parameters for the 10 different electron configurations at a single site. These are given by $|0\rangle$, $|A^{\sigma}\rangle$, $|B^{\sigma}\rangle$, $|A^{\sigma}B^{\bar{\sigma}}\rangle$, $|A^{\sigma}B^{\sigma}\rangle$, $|B^{\uparrow}B^{\downarrow}\rangle$, $|A^{\uparrow}A^{\downarrow}\rangle$, $|A^{\sigma}B^{\uparrow}B^{\downarrow}\rangle$, $|A^{\uparrow}A^{\downarrow}B^{\sigma}\rangle$, $|A^{\uparrow}A^{\downarrow}B^{\uparrow}B^{\downarrow}\rangle$ with $\sigma=\uparrow$ and $\downarrow$, where $A^{\sigma}(B^{\sigma})$ implies that the A (B) orbital is occupied by the σ spin electron. The fixed-sampling method is used to optimize the variational parameters.[25] In addition to the standard VMC method, we improve the variational wave function by estimating analytically the weights for the configurations which are sampled by the Monte Carlo (MC) simulations. This method is valid for the LS state and reduces the computational time by more than one order of magnitude. In most of the calculations, 10^4-10^5 MC samples are used for measurement.

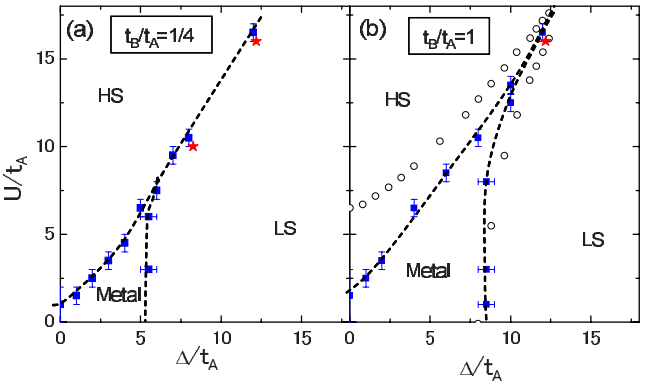

FIG. 1. (Color online) Phase diagrams at $x=0$. The ratio of the electron transfers is taken to be $t_B/t_A=1/4$ in (a) and $t_B/t_A=1$ in (b). In (b), the filled squares and open circles show the results obtained by the VMC method and the previous DMFT method in Ref. 21, respectively. The broken curves are guides for the eyes. The stars represent the parameters where the carrier dopings were examined.

III. RESULTS AND DISCUSSION

We start from the case at $x=0$ where the average electron number per site is two. The electronic states obtained by the simulation are monitored by the total spin amplitude defined by $\mathbf{S}^2=(1/N)\Sigma_i\langle \mathbf{S}^2_i\rangle$, where $\mathbf{S}_i=\Sigma_{\gamma}\mathbf{S}_{i\gamma}=(1/2)\Sigma_{ss',\gamma}c^{\dagger}_{i\gamma s}\boldsymbol{\sigma}_{ss'}c_{i\gamma s'}$ is the spin operator with Pauli matrices $\boldsymbol{\sigma}$, the spin correlation function $S_{\gamma}(\mathbf{q})=(4/N^2)\Sigma_{ij}e^{i\mathbf{q}\cdot(\mathbf{r}_i-\mathbf{r}_j)}\langle S^z_{i\gamma}S^z_{j\gamma}\rangle$, and the momentum-distribution function $n_{\gamma}(\mathbf{k})=(1/2)\Sigma_{\sigma}\langle c^{\dagger}_{\mathbf{k}\gamma\sigma}c_{\mathbf{k}\gamma\sigma}\rangle$. We obtain three phases, the HS-Mott insulator (MI), the LS-BI and the metallic (ML) phases. In the HS-MI phase, $\mathbf{S}^2$ is about 1.6, being about 80% of the maximum value for $S=1$. A sharp peak in $S_{\gamma}(\mathbf{q})$ at $\mathbf{q}=(\pi,\pi)$ and no discontinuity in $n_{\gamma}(\mathbf{k})$ imply that this is the AFM-MI phase. In the LS-BI phase, $n_A(\mathbf{k})$ and $n_B(\mathbf{k})$ are almost zero and one, respectively, for all momenta, and $\mathbf{S}^2 \simeq 0$. In the ML phase, discontinuous jumps are observed in both $n_A(\mathbf{k})$ and $n_B(\mathbf{k})$. The electron and hole Fermi surfaces are located around $\mathbf{k}=(0,0)$ and (π,π) in the A and B band, respectively. This is a semimetal. The value of $\mathbf{S}^2$ is about 0.3 and no remarkable structure is seen in $S_{\gamma}(\mathbf{q})$. The size dependences of $\mathbf{S}^2$ and $S_{\gamma}(\mathbf{q})$ in $L=4-8$ are within a few percent in both the HS-MI and ML phases. In the LS-BI phase, the total energy increases about 0.5 percent by changing the system size from $L=4$ to 8.

The phase diagram at $x=0$ is shown in Fig. 1. The error bars imply the upper and lower bounds of the phase boundary; symbols are plotted at the center of the bars. The LS-BI

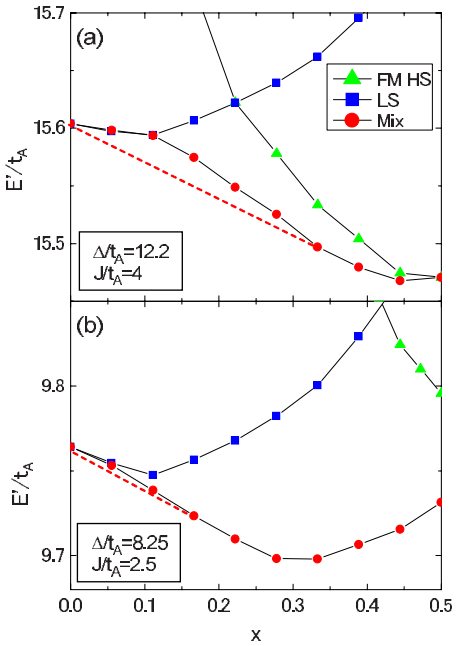

FIG. 2. (Color online) Hole concentration dependences of the energy expectations for several states at $(\Delta/t_A, J/t_A)=(12.2,4)$ in (a), and at $(\Delta/t_A, J/t_A)=(8.25,2.5)$ in (b). The broken lines are given by the Maxwell's construction. The ratio of the electron transfers is taken to be $t_B/t_A=1/4$. The constant parameter C in the definition of E' is taken to be 16.4 in (a) and 10.5 in (b).

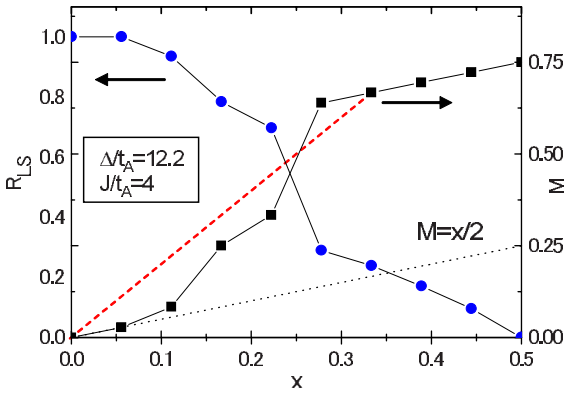

FIG. 3. (Color online) Ratio of LS sites to LS and HS sites in the mixed state, R_{LS}, and magnetization $M(x)$ as functions of the hole concentration x. The broken line connecting the data at $M(x=0)$ and $M(x=0.33)$ is drawn by Maxwell's rule. For comparison, we plot the $M(x)=x/2$ curve expected from the hole doping in the LS-BI phase. The parameters are chosen to be $(\Delta/t_A, J/t_A)=(12.2,4)$ and $t_B/t_A=1/4$.

and HS-MI phases are realized in the regions of large Δ and J, respectively. The ML phase appears between the regions of small Δ and J. To compare the present results with previous results calculated by the dynamical-mean field theory (DMFT),[21] in Fig. 1(b), we present the phase diagram where the two transfer integrals are chosen to be equal, $t_B/t_A=1$. Although the global features in the phase diagrams are the same, the HS-MI phase obtained by the VMC method appears in a broader parameter region than that for DMFT, in particular, near the boundary of the HS-MI and ML phases. This is because the AFM long-range order in the HS-MI phase is treated properly in the VMC method. We have confirmed that the phase boundaries obtained by the VMC method where the AFM order is not considered almost reproduce the DMFT results.

Now we show the results at finite x. Holes are introduced into the LS-BI phase near the phase boundary with the parameter values of $(\Delta/t_A, J/t_A)=(12.2,4)$ and $(8.25,2.5)$ [see Fig. 1]. By changing the one-body wave function $|\Phi\rangle$ and the initial conditions of the variational parameters in the VMC simulation, we obtain the following four states: (i) the LS-ML state where $n_A(\mathbf{k})$ is almost zero for all $\mathbf{k}$, and the Fermi surface is located in the B band around $\mathbf{k}=(\pi,\pi)$, (ii) the FM HS-ML state where $n_B(\mathbf{k})$ is about 1/2 in all $\mathbf{k}$, the Fermi surface is in the A band, and $S_\gamma(\mathbf{q})$ has a sharp peak at $\mathbf{q}=(0,0)$, (iii) the AFM HS-ML state where the Fermi surface exists in the A band around $\mathbf{k}=(\pi,0)$, and $S_\gamma(\mathbf{q})$ has a peak at $\mathbf{q}=(\pi,\pi)$, and iv) the mixed state where three kinds of the on-site electron configurations, $|B^2\rangle$, $|A^1B^1\rangle$ with $S=1$, and $|B^1\rangle$, are distributed spatially.

In Fig. 2(a), the energy expectation values $E\equiv\langle\mathcal{H}\rangle$ for the several states in $(\Delta/t_A, J/t_A)=(12.2,4)$ are plotted as functions of x. The transfer integrals are chosen to be $t_B/t_A=1/4$. To show the numerical data clearly, we plot $E'=(E/t_A)+Cx$ with a numerical constant C instead of E. This transformation does not affect the Maxwell's construction introduced below. We also analyze the PS state by a function[16] $\varepsilon(x)\equiv[E(x)-E(x=0)]/x$ and the obtained results are consistent in the two methods. The results for the AFM HS-ML are not plotted, because their energy values are higher than the others within the energy scale presented in the figures. In Fig. 3, we present the ratio of the LS sites to the LS and HS sites in the mixed states defined by $R_{LS}=n_{LS}/(n_{LS}+n_{HS})$. Here, n_{LS} and n_{HS} are the number of sites where the LS and HS states, respectively, are realized. As shown in Fig. 2(a), the LS state, where holes are doped into the B band, is destabilized monotonically with increasing x. In the region of $x\geq 0.5$, the FM HS-ML state is realized. In between the two regions, the mixed state is the lowest energy state. The mixed state is smoothly connected to the LS and HS states in the low and high x regions, respectively. As shown in Fig. 3, a discontinuous jump in the mixed state is seen around $x=0.25$; the system changes from an LS dominant mixed state into an HS dominant state with x. It is noticeable that the E' versus x curve in the mixed state is convex in the region of $0<x<0.33$. That is, by following Maxwell's construction, the PS of the LS-BI and the FM HS dominant mixed states is more stabilized than the homogeneous phase in this region of x. In Fig. 2(b), we show the results for $(\Delta/t_A, J/t_A)=(8.25,2.5)$ where the system at $x=0$ is close to the ML phase [see Fig. 1(a)]. The PS appears, but its region is shrunk.

The magnetization per site in the lowest energy state defined by $M(x)=(1/N)\langle\Sigma_i S_i^z\rangle$ is plotted in Fig. 3. The zero magnetization at $x=0$ reflects the LS-BI ground state. In the high-doped region of $x>0.33$, the magnetization data almost follows the relation $M(x)\simeq(1+x)/2$. The system is expected to consist of $N/2$ HS sites, $(1/2-x)N$ LS sites, and xN singly-electron occupied sites. In this scheme, we obtain

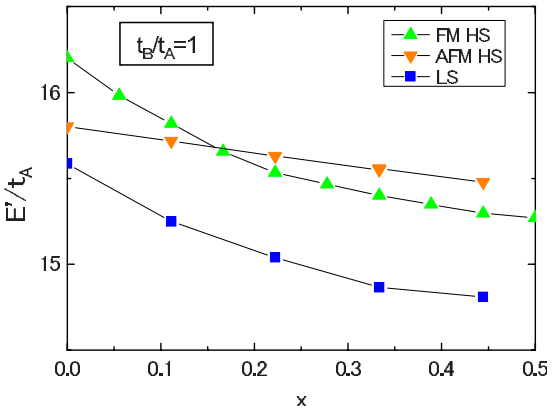

FIG. 4. (Color online) Hole concentration dependences of the energy expectations for several states where the electron transfer integrals are chosen to be equal as $t_B/t_A=1$. The other parameters are taken to be $(\Delta/t_A, J/t_A)=(12.2, 4)$, and the constant parameter C in the definition of E' is taken to be 16.

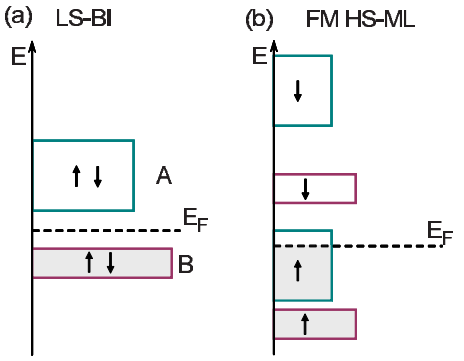

FIG. 5. (Color online) Schematic density-of-states in the LS-BI state at $x=0$ and that in the HS-ML state in a high hole-doped region.

$R_{LS}=(1-2x)/(2-2x)$, which is consistent with the numerical data of R_{LS} for $x>0.33$. Between $x=0$ and 0.33, where the PS is realized, $M(x=0)$ and $M(x=0.33)$ are connected by a straight line according to the volume-fraction rule in Maxwell's construction. The slope of $M(x)$ is about three times higher than $M(x)=x/2$, which is expected in the hole doping in the LS-BI phase. This is qualitatively consistent with the experimental observations of the magnetization where doped holes induce high-spin values.[3,26]

We now address the origin of the electronic PS where the spin-state degree of freedom is concerned. In Fig. 4, we present the hole concentration dependence of the energy expectations where the band widths are set to be equal, $t_B/t_A=1$. The energy parameters are taken to be $(\Delta/t_A, J/t_A)=(12.2, 4)$, which are same with that in the calculation shown in Fig. 2(a) and are close to the LS-HS phase boundary at $x=0$ [see Fig. 1(b)]. The mixed state is not obtained in the simulation. In all regions of x up to $x=0.45$, the LS state is the lowest ground state, and neither the spin-state transition nor the PS occur. The difference of the band widths in the two orbitals is essential in the electronic PS phenomena.[27]

Schematic diagrams of the density of states in the LS-BI at $x=0$ and the FM HS-ML in a high hole-doped region are presented in Fig. 5. In the LS-BI state at $x=0$, the Fermi level (FL) is located inside the band gap between the A and B bands. The band width of the A band is larger than that of B. On the other hand, in the FM HS-ML state, which is realized for $x \gtrsim 0.5$ in Fig. 2(a), the system is a doped MI with FM spin polarization. The FL is located in the A band. Because of the large band width of the A band, there is a large kinetic energy gain in comparison with the doped LS-BI state where the FL is located in the B band in the rigid band scheme. This kinetic energy gain is the origin of the spin state transition by doping. It is shown in Fig. 4 that when equal band widths are assumed, the E' vs x curves for the LS-ML and FM HS-ML states are almost parallel and do not cross. This result implies that there is no difference in the kinetic energy gains for the two states when the band widths are assumed to be equal. The present PS phenomena are also attributed to this band width difference as follows. In the rigid-band sense, by doping of holes in the LS-BI state, the FL falls into the top of the B band from the middle of the gap in Fig. 5(a). If we suppose that this state is realized in a low x region and is transferred into the FM HS-ML state shown in Fig. 5(b) with increasing x, the FL is increased with increasing hole concentration because of the different band widths. This implies the negative charge compressibility $\kappa=-(\partial\mu/\partial x)<0$ with the chemical potential μ, i.e., the appearance of the electronic PS.

Finally, we discuss the implications for perovskite cobaltites. The obtained PS between the insulating nonmagnetic state and the hole-rich FM state provides an interpretation for the inhomogeneity observed in a number of experiments. The PS and the spin-state transition are attributed to the bandwidth difference of the two bands corresponding to the e_g and t_{2g} bands in the perovskite cobaltites. This electronic PS is robust under changes in the model parameter values, except for t_B/t_A, when the nondoped system is located near the phase boundary between the LS-BI and HS-MI. Our scenario of the PS based on the bandwidth difference may be checked experimentally by adjusting the tolerance factor, i.e., the Co-O-Co bond angle. A smaller tolerance factor implies a smaller or larger band width in the e_g or t_{2g} orbitals, respectively, and suppression of the PS. Detailed values of x where the PS is realized and a typical size of the clusters remain unanswered questions. Several factors not considered here, the intermediate-spin state, the long-range Coulomb interaction, the lattice volume depending on the spin states, and others, are required to answer these questions.

ACKNOWLEDGMENTS

The authors would like to thank H. Yokoyama and H. Takashima for their valuable discussions. This work was supported by JSPS KAKENHI, TOKUTEI from MEXT, and Grand Challenges in Next-Generation Integrated Nanoscience.

*Present address: The Bank of Tokyo-Mitsubishi UFJ, Tokyo, Japan.

†Present address: Chiba Institute of Technology, Tsudanuma, Chiba 275-0016, Japan.

[1] S. Maekawa, T. Tohyama, S. Barnes, S. Ishihara, W. Koshibae, and G. Khalliulin, *Physics of Transition Metal Oxides* (Springer Verlag, Berlin, 2004) (and references therein).

[2] M. Imada, A. Fujimori, and Y. Tokura, Rev. Mod. Phys. **70**, 1039 (1998).

[3] S. Yamaguchi, Y. Okimoto, H. Taniguchi, and Y. Tokura, Phys. Rev. B **53**, R2926 (1996).

[4] M. A. Korotin, S. Y. Ezhov, I. V. Solovyev, V. I. Anisimov, D. I. Khomskii, and G. A. Sawatzky, Phys. Rev. B **54**, 5309 (1996).

[5] M. W. Haverkort, Z. Hu, J. C. Cezar, T. Burnus, H. Hartmann, M. Reuther, C. Zobel, T. Lorenz, A. Tanaka, N. B. Brookes, H. H. Hsieh, H.-J. Lin, C. T. Chen, and L. H. Tjeng, Phys. Rev. Lett. **97**, 176405 (2006).

[6] S. Noguchi, S. Kawamata, K. Okuda, H. Nojiri, and M. Motokawa, Phys. Rev. B **66**, 094404 (2002).

[7] Y. Kobayashi, T. S. Naing, M. Suzuki, M. Akimitsu, K. Asai, K. Yamada, J. Akimitsu, P. Manuel, J. M. Tranquada, and G. Shirane, Phys. Rev. B **72**, 174405 (2005).

[8] M. Itoh, I. Natori, S. Kubota, and K. Motoya, J. Phys. Soc. Jpn. **63**, 1486 (1994).

[9] R. Caciuffo, D. Rinaldi, G. Barucca, J. Mira, J. Rivas, M. A. Senãrís-Rodríguez, P. G. Radaelli, D. Fiorani, and J. B. Goodenough, Phys. Rev. B **59**, 1068 (1999).

[10] P. L. Kuhns, M. J. R. Hoch, W. G. Moulton, A. P. Reyes, J. Wu, and C. Leighton, Phys. Rev. Lett. **91**, 127202 (2003).

[11] A. Ghoshray, B. Bandyopadhyay, K. Ghoshray, V. Morchshakov, K. Bärner, I. O. Troyanchuk, H. Nakamura, T. Kohura, G. Y. Liu, and G. H. Rao, Phys. Rev. B **69**, 064424 (2004).

[12] J. Wu, J. W. Lynn, C. J. Glinka, J. Burley, H. Zheng, J. F. Mitchell, and C. Leighton, Phys. Rev. Lett. **94**, 037201 (2005).

[13] D. Phelan, S. Despina Louca, S. Rosenkranz, S.-H. Lee, Y. Qiu, P. J. Chupas, R. Osborn, H. Zheng, J. F. Mitchell, J. R. D. Copley, J. L. Sarrao, and Y. Moritomo, Phys. Rev. Lett. **96**, 027201 (2006).

[14] D. Phelan, D. Louca, K. Kamazawa, S.-H. Lee, S. Rosenkranz, M. F. Hundley, J. F. Mitchell, Y. Motome, S. N. Ancona, and Y. Moritomo, Phys. Rev. Lett. **97**, 235501 (2006).

[15] For reviews, see for examples, S. A. Kivelson, I. P. Bindloss, E. Fradkin, V. Oganesyan, J. M. Tranquada, A. Kapitulnik, and C. Howald, Rev. Mod. Phys. **75**, 1201 (2003); E. Dagotto, *The Physics of Manganites and Related Compounds* (Springer-Verlag, Berlin, 2003).

[16] V. J. Emery, S. A. Kivelson, and H. Q. Lin, Phys. Rev. Lett. **64**, 475 (1990).

[17] E. L. Nagaev, Phys. Status Solidi B **186**, 9 (1994).

[18] S. Okamoto, S. Ishihara, and S. Maekawa, Phys. Rev. B **61**, 451 (2000).

[19] K. I. Kugel, A. L. Rakhmanov, and A. O. Sboychakov, Phys. Rev. Lett. **95**, 267210 (2005).

[20] M. Lugas, L. Spanu, F. Becca, and S. Sorella, Phys. Rev. B **74**, 165122 (2006).

[21] P. Werner and A. J. Millis, Phys. Rev. Lett. **99**, 126405 (2007).

[22] K. Sano and Y. Ono, J. Phys. Soc. Jpn. **72**, 1847 (2003).

[23] K. Kobayashi and H. Yokoyama, Physica C **445-448**, 162 (2006).

[24] K. Kubo, Phys. Rev. B **79**, 020407(R) (2009).

[25] C. J. Umrigar, K. G. Wilson, and J. W. Wilkins, Phys. Rev. Lett. **60**, 1719 (1988).

[26] J. Okamoto, H. Miyauchi, T. Sekine, T. Shidara, T. Koide, K. Amemiya, A. Fujimori, T. Saitoh, A. Tanaka, Y. Takeda, and M. Takano, Phys. Rev. B **62**, 4455 (2000).

[27] A relation between the band widths and PS is also studied by A. O. Sboychakov, K. I. Kugel, and A. L. Rakhmanov, Phys. Rev. B **76**, 195113 (2007).